Electronic Supplementary Information

Novel Fe_2O_3 microspheres composed of triangular star-shaped nanorods as electrode for supercapacitors

Zhiting Song[a], Hongming Hu[a], Kai Shu[a], Tao Liu[a], Xiao Tang[a], Xianju Zhou[a], Yanhong Li[a*],

Yunhuai Zhang[b*]

[a]*College of Science, Chongqing University of Posts and Telecommunications, Chongqing, 400065, P. R. China*

[b]*College of Chemistry and Chemical Engineering, Chongqing University, Chongqing, 400044, P. R. China*

Corresponding Author's Email: liyanhong@cqupt.edu.cn; xp2031@163.com

Experimental Part

Materials

Carbon cloth was purchased from Shanghai Hesen Electrical Co., Ltd. KOH and $FeCl_3$ were purchased from Shanghai Macklin Biochemical Co., Ltd. HNO_3 and urea were purchased from Chongqing Chuandong Chemical (Group) Co., Ltd. Sublimed sulfur was purchased from Shanghai Aladdin Biochemical Technology Co., Ltd. Thiourea was purchased from Yixing Kelong Chemical Co., Ltd. Ascorbic acid was purchased from Guangdong Guanghua Sci-Tech Co., Ltd. The reagents were of analytical grade and used without further purification.

Fe_2O_3-S/AAC composite preparation

Typically, the carbon cloth was immersed in HNO_3 for 24 hours before use to improve the

surface hydrophilicity of carbon cloth, and therefore facilitate heterogeneous nucleation of ions during the hydrothermal process, which would helpful for the growth of precursor. After washing the above carbon cloth with anhydrous ethanol and ultrapure water, respectively, it was dried in air at 60 °C for 12 hours to obtain activated carbon cloth (ACC). The synthesis of Fe_2O_3 on the carbon cloth was carried out *via* a hydrothermal method. Specifically, 0.4866 g of $FeCl_3$, 0.4504 g of urea, and 0.5282 g of ascorbic acid were dissolved in 30 mL of ultrapure water (UPW). The homogeneous solution was transferred into a 50 mL Teflon-lined stainless-steel autoclave, and a piece of ACC (1 × 4 cm) was immersed in the solution. The autoclave was then sealed and put into an electric oven. After maintaining at 180 °C for 4 hours, the carbon cloth was washed with deionized water and ethanol, respectively, and dried at 60 °C for 12 hours. Fe_2O_3 grown on activated carbon cloth (Fe_2O_3/ACC) was obtained by annealing the carbon cloth at 400 °C for 3 hours. Furthermore, the Fe_2O_3/ACC was treated with sublimed sulfur in a nitrogen atmosphere at 350 °C for 2 hours to obtain S-doped Fe_2O_3 carbon cloth (Fe_2O_3-S/ACC).

Characterizations

The surface morphology of the samples was characterized using a scanning electron microscope (SEM, Apreo 2C, Thermo Scientific) and a transmission electron microscope (TEM, Talos F200X G2, Thermo Scientific). X-ray diffraction (XRD) patterns were obtained employing an X-ray diffraction instrument (XRD, XD-2, Persee). The chemical properties of the materials were analyzed using an X-ray photoelectron spectrometer (XPS, ESCALAB Xi+, Thermo Scientific). The plasma mass spectrometer (ICP-MS, ICAP RQ, Thermo Scientific) was used to characterize the ion concentrations. N_2 adsorption-desorption isotherms measurement was carried out on a full-automatic physical adsorption instrument (ASAP 2460, Micromeritics) to analyze the surface and pore structure.

The 4-point probe technique (Four Probe Resistivity Tester, RTS-9, 4Probes Tech Ltd.) was used to measure the macroscopic resistivity/resistance.

Electrochemical measurements

To evaluate the electrochemical performance of the synthesized Fe_2O_3-S/ACC composite material, a three-electrode system was used with Pt metal as the counter electrode and Hg/HgO as the reference electrode, respectively. The electrolyte used for all electrochemical tests was a 1M KOH aqueous solution. The electrochemical techniques employed in this study included cyclic voltammetry (CV), galvanostatic discharge/charge (GCD) and electrochemical impedance spectroscopy (EIS). All measurements were conducted on a workstation (CHI660E, Chenhua, Shanghai). Additionally, the cycling stability test was performed on a LAND battery system. The areal specific capacitance was calculated using the equation as follows:

$$C = I \times \Delta t/(s \times \Delta V) \#(1)$$

Where I is the constant discharging current, Δt is the discharging time, ΔV is the voltage and s is the effective area of electrode. Asymmetric supercapacitors with Fe_2O_3-S/ACC as negative and NiCo-PBA as positive electrode were assembled and the mass ratio between them was calculated based on the charge balance theory equations below[1]. The glass fiber paper (Whatman) was used as separator and 1M KOH was employed as electrolyte.

$$Q_+ = Q_- \#(2)$$

$$\frac{m_+}{m_-} = \frac{C_{s-} \times \Delta V_-}{C_{s+} \times \Delta V_+} \#(3)$$

Here Q, Cs, m, and ΔV represented the charges, specific capacitance, mass loading and potential window, respectively. "+" and "–" represented the positive and negative electrode, respectively.
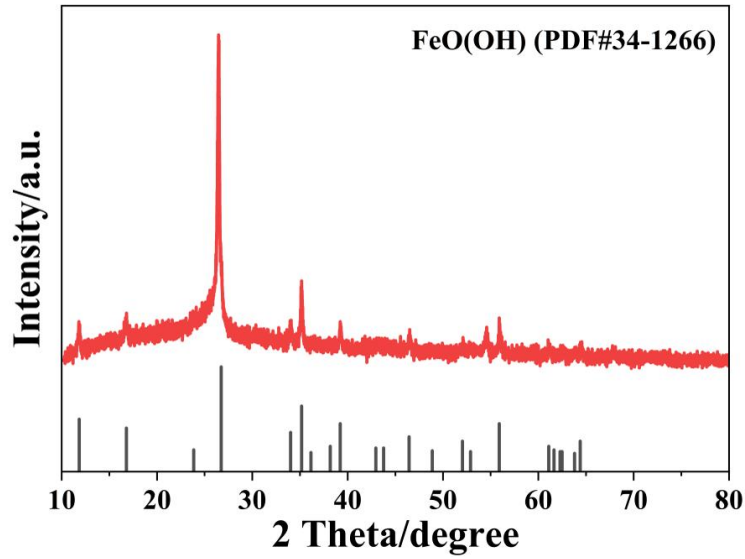
Fig. S1 XRD pattern of precursors.

To identify the phase of the precursor and avoid the influence of the substrate (carbon cloth), the powder sample was used to conduct XRD test, and the results were shown in Fig. S1. It could be seen that the XRD pattern displayed characteristic peaks that matched well with the FeO(OH) (PDF card no: 34-1266) after hydrothermal process and no other obvious peaks were observed.
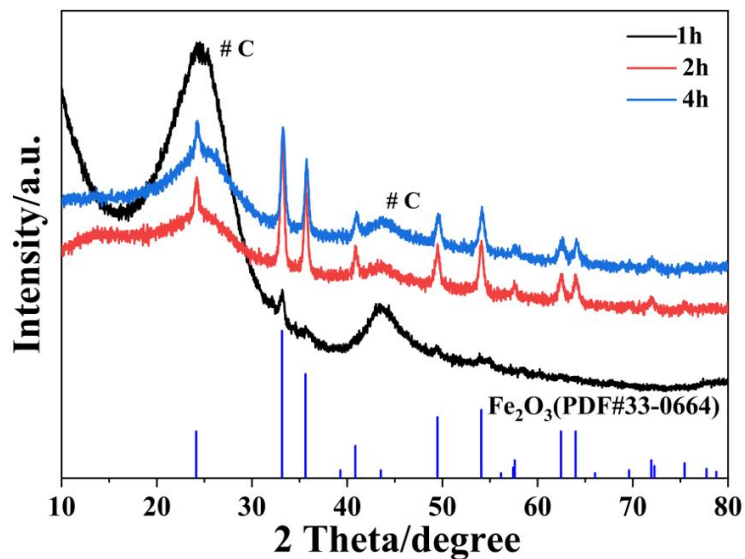

Fig. S2 XRD pattern of Fe_2O_3/ACC under different hydrothermal reaction times.

The XRD test was conducted on Fe_2O_3/ACC under different hydrothermal times to investigate the phase changes during the reaction and the results were shown in Fig. S2. It was obvious that when the reaction time was 1 hour, the XRD pattern exhibited weak characteristic peaks of Fe_2O_3 due to the low content of materials grown on the carbon cloth. As the hydrothermal time was extended to more than 2 hours, the XRD pattens showed distinct and well-defined peaks of Fe_2O_3.
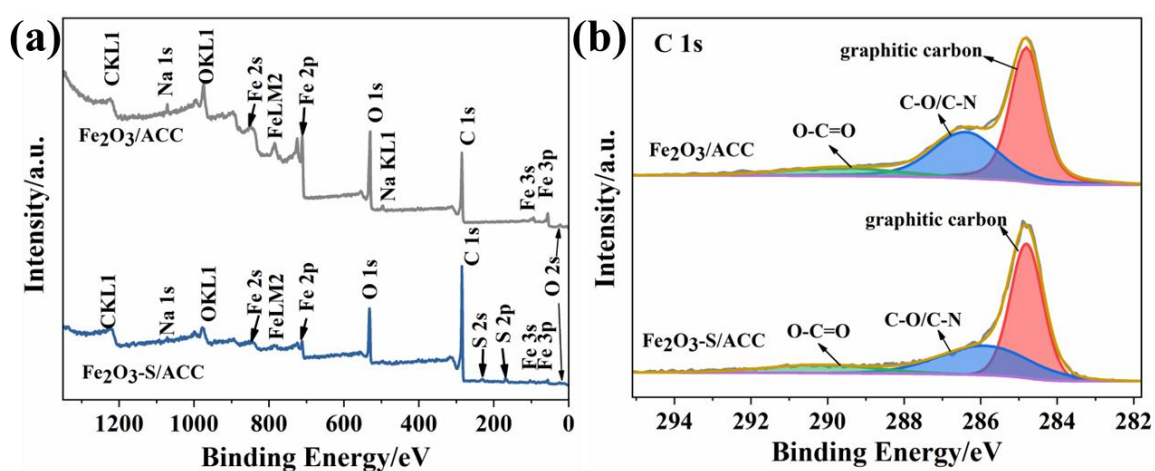

Fig. S3 XPS spectra of Fe_2O_3/ACC and Fe_2O_3-S/ACC. (a) XPS survey; (b) C 1s.

Table S1 XPS fitting results of Fe_2O_3/ACC and Fe_2O_3-S/ACC.

Sample/binding energies / Fitting peaks	Fe_2O_3/ACC/eV	Fe_2O_3-S/ACC/eV
Fe(III) Fe 2p3/2	711.33	711.58
Fe(III) of Fe 2p1/2	724.77	725
Fe(II) of Fe 2p3/2	709.98	710.24
Fe(II) of Fe 2p1/2	723.11	723.47
C 1s (graphitic carbon)	284.8	284.8
C 1s (C-O/C-N)	286.4	285.89
C 1s (O-C=O)	289.64 eV	290.17
O 1s (lattice oxygen)	530.1	530.57
O 1s (hydroxyl oxygen)	531.33	531.94

O 1s (adsorbed oxygen)	533	533.37
S(-II) of S 2p3/2	/	163.65
S(0) of S 2p1/2	/	164.95
S(IV)/S(VI)	/	168.6

Table S2 Atomic proportion in Fe_2O_3-S/ACC based on XPS results.

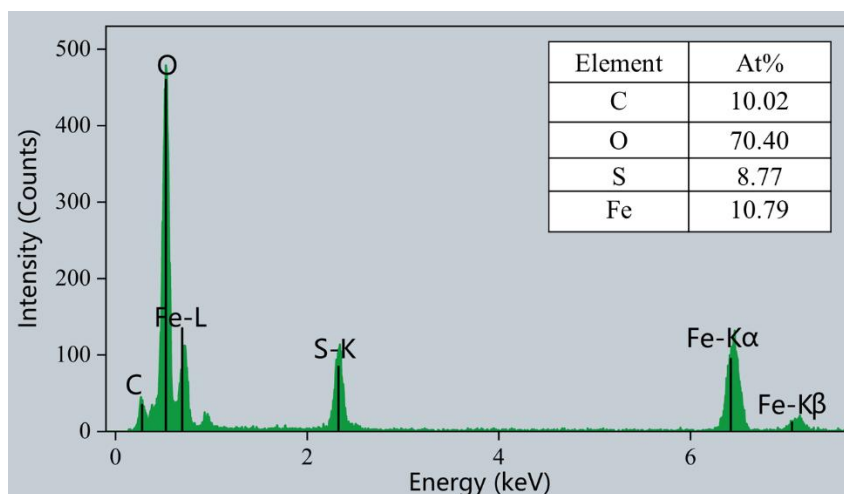| Element	Atomic %
C 1s	76.89
O 1s	17.24
Fe 2p	3.46
S 2p	2.41

Fig. S4 Atomic proportion of Fe_2O_3-S/ACC based on EDX results.

XPS and EDS analysis was performed to estimate the atomic concentration of sulfur and the result were shown in Table S2 and Fig. S4. The calculated atomic ratio of Fe:S was 1.41 and 1.23, respectively.
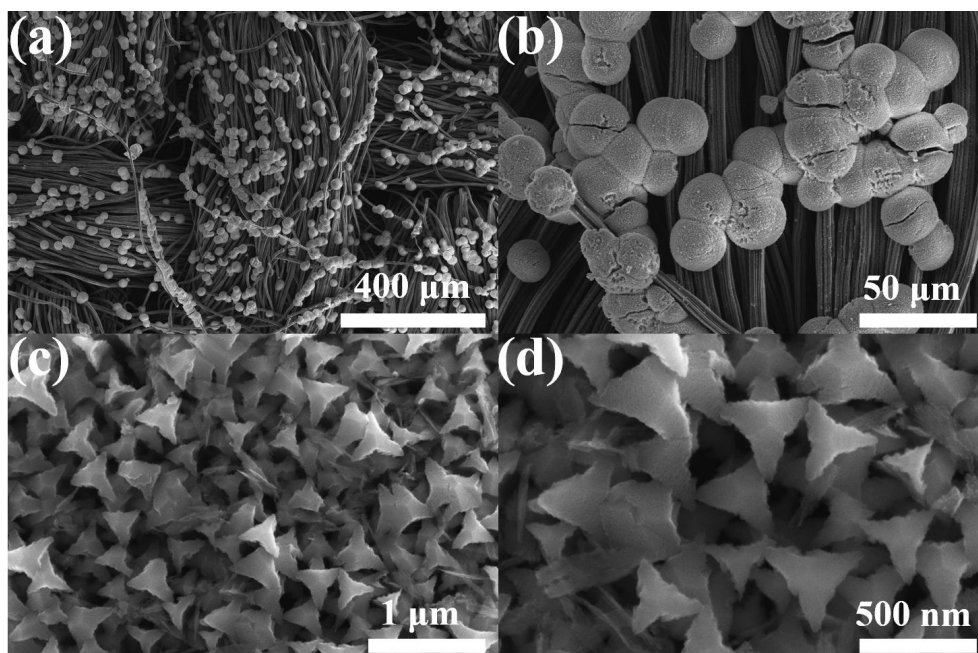
Fig. S5 SEM images of Fe₂O₃/ACC.

Table S3 The macroscopic resistivity values of Fe₂O₃/ACC by 4-poitn probe technique.

Fe₂O₃/ACC							
Range (mA)	Current (mA)	Mean Probe Spacing (mm)	Diameter (mm)	Diameter Correction Factor	Thickness (mm)	Thickness Correction Factor	Probe Spacing Correction Factor
10	9.999	1	25	4.47	0.3	1	1
Test Data							
point	X(mm)	Y(mm)	Forward voltage (mV)	Reverse voltage (mV)	Resistivity (Ω·cm)	Conductivity (s/cm)	
1	0	0	10.61	10.61	0.142	7.042	
2	0	-6.25	13.87	13.87	0.184	5.435	
3	0	6.25	10.77	10.76	0.143	6.993	
4	0	0	10.01	10.01	0.134	7.463	
5	0	0	10.03	10.02	0.134	7.463	
Analysis data (Resistivity Ω·cm)							
Maximum			Minimum			**Average**	
0.184			0.134			**0.1474**	

Table S4 The macroscopic resistivity values of Fe$_2$O$_3$-S/ACC by 4-poitn probe technique.

Fe$_2$O$_3$-S/ACC							
Range (mA)	Current (mA)	Mean Probe Spacing (mm)	Diameter (mm)	Diameter Correction Factor	Thickness (mm)	Thickness Correction Factor	Probe Spacing Correction Factor
10	10	1	25	4.47	0.3	1	1
Test Data							
point	X(mm)	Y(mm)	Forward voltage (mV)	Reverse voltage (mV)	Resistivity (Ω·cm)	Conductivity (s/cm)	
1	0	0	5.1	5.09	0.068	14.71	
2	0	-6.25	4.99	4.98	0.066	15.15	
3	0	6.25	4.81	4.8	0.064	15.63	
4	0	0	4.69	4.68	0.063	15.87	
5	0	0	4.69	4.67	0.063	15.87	
Analysis data (Resistivity Ω·cm)							
Maximum			Minimum			**Average**	
0.068			0.063			**0.0648**	

Macroscopic resistivity using a 4-point probe technique was conducted and the results were shown in Table S3 and Table S4. These tables presented the test conditions and the measured macroscopic resistivity values for both Fe$_2$O$_3$-S/ACC and Fe$_2$O$_3$/ACC samples. It was clear that the average resistivity for Fe$_2$O$_3$-S/ACC and Fe$_2$O$_3$/ACC was 0.0648 Ω·cm and 0.1474 Ω·cm, respectively. The results demonstrated that Fe$_2$O$_3$-S/ACC exhibited lower resistivity and better conductivity compared to Fe$_2$O$_3$/ACC, which could contribute to more efficient electron transfer.
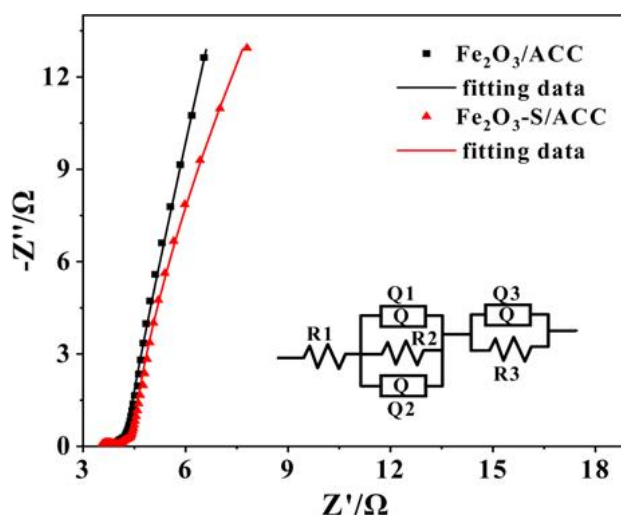
Fig. S6 The EIS test and fitting results of Fe_2O_3/ACC and Fe_2O_3-S/ACC. The inset is the equivalent circuit.
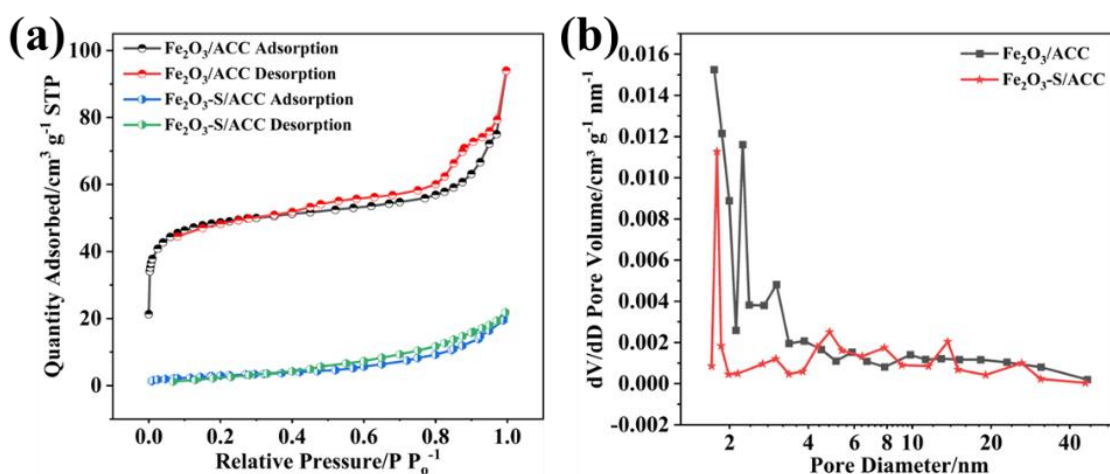

Fig. S7 N_2 adsorption-desorption isotherms and BJH pore size distribution results of Fe_2O_3/ACC and Fe_2O_3-S/ACC, respectively.

N_2 adsorption-desorption isotherms measurement was conducted to get the porous structural information of samples and the results were shown in Fig. S7. The BET (Brunauer-Emmett-Teller) results (Fig. S7) showed that the specific surface area of Fe_2O_3/ACC and Fe_2O_3-S/ACC was 185.6 m²/g and 9.2 m²/g, respectively. The pore size distribution curve obtained from the BJH (Barrett Joyner-Halenda) method confirmed the narrow pore size distribution of Fe_2O_3-S/ACC. Therefore,

Fe$_2$O$_3$/ACC not only exhibited much larger specific area than that of Fe$_2$O$_3$-S/ACC, but also wider pore size distribution, which would be more beneficial for easier access of electrolyte.
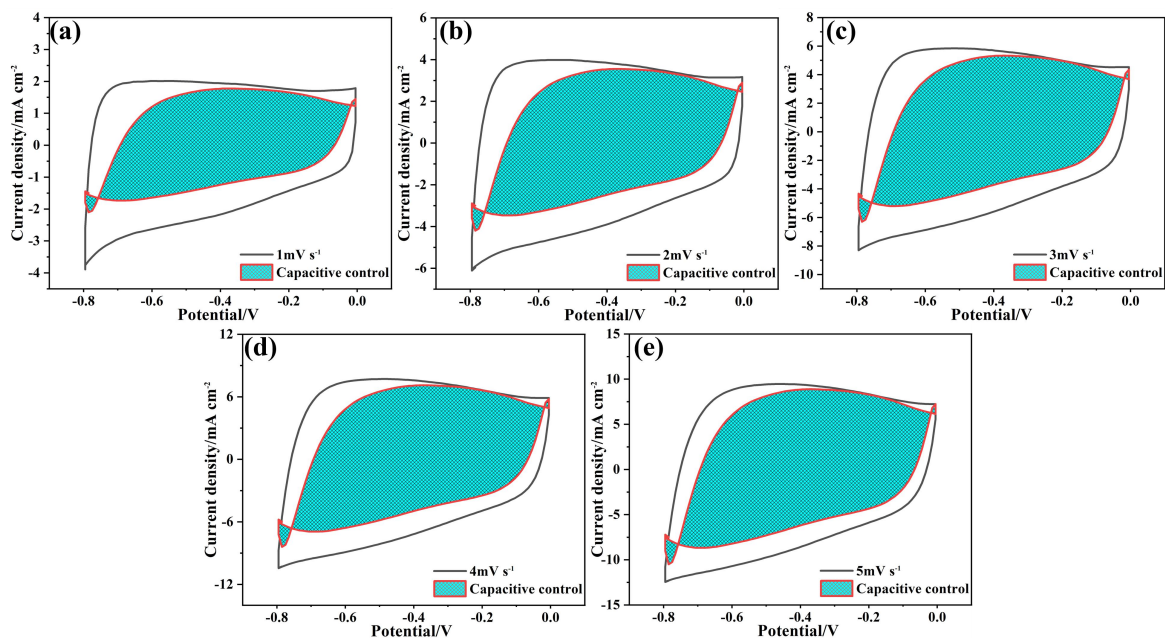

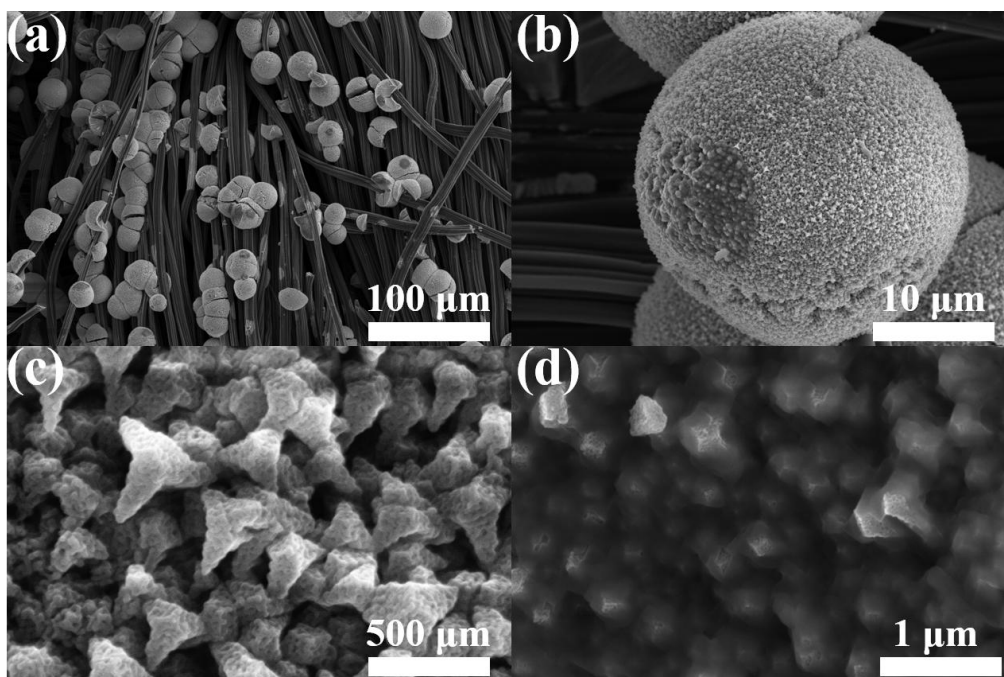**Fig. S8** Capacitance contributions of Fe$_2$O$_3$-S/ACC under different scan rates.

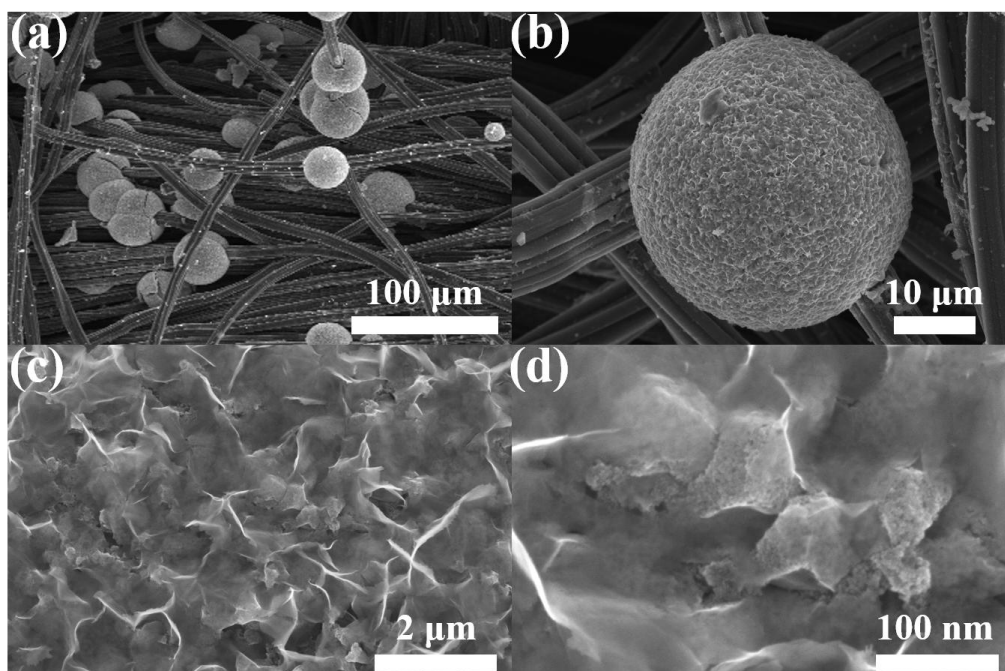**Fig. S9** SEM images of Fe$_2$O$_3$/ACC after cycling test.

Fig. S10 SEM images of Fe$_2$O$_3$-S/ACC after cycling test.

The SEM results of both samples after cycling test were presented in Fig. S9 and S10. It could be seen that after cycling test Fe$_2$O$_3$/ACC maintained triangular star-shaped structure with a rougher surface. On the other hand, although the triangular star-shaped structure was still visible in Fe$_2$O$_3$-S/ACC, it was covered with a layer of sheet-like materials (Fig. S10c and d). The degradation of the capacitance could be ascribed to the formation of the sheet-like structure at the surface of Fe$_2$O$_3$-S/ACC, which was unfavorable for the access of electrolyte ions.

Table S5 ICP results of electrolyte after cycling test.

Sample (electrolyte)	Fe concentration (ng/ml)
Fe$_2$O$_3$/ACC	186.39
Fe$_2$O$_3$-S/ACC	514.53

ICP measurement was conducted to further investigated the capacitance fading of Fe$_2$O$_3$-S/ACC.

It could be seen that a more severe dissolution of active materials was observed in Fe_2O_3-S/ACC, which could be the reason for its capacitance degradation.
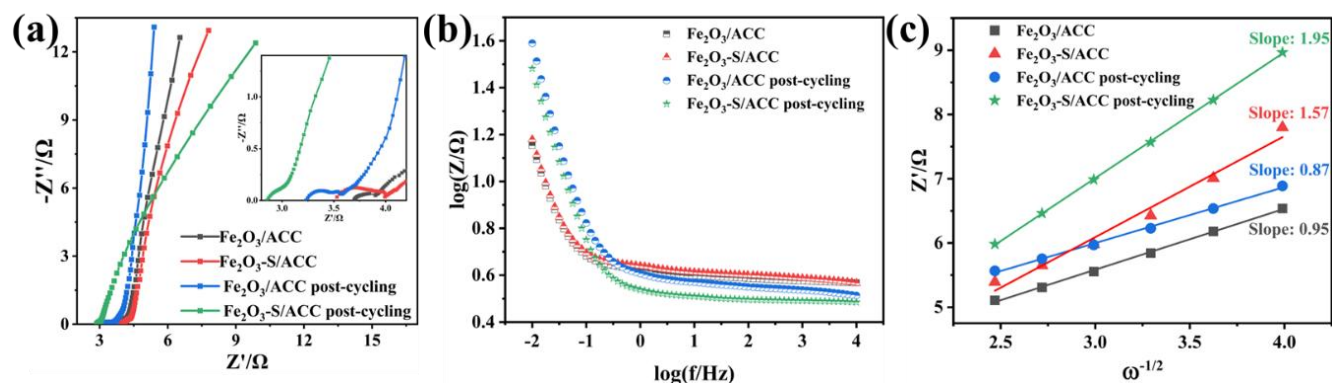

Fig. S11 EIS results of Fe_2O_3/ACC and Fe_2O_3-S/ACC before and after cycling test.

EIS test was also conducted to identify the capacitance loss of Fe_2O_3-S/ACC and the results were shown in Fig. S11. It could be seen that though the R_s of both electrodes decreased after cycling tests, the overall impedance increased in low frequency region (diffusion-controlled or mass transfer process) and decreased in high frequency region (kinetics-controlled or charge transfer process), which demonstrated the easier charge transfer and harder ion transfer after cycling test, respectively. And this was more obvious for Fe_2O_3-S/ACC as the curves before and after cycling tests showed bigger difference compared to that of Fe_2O_3/ACC. The above results were confirmed by the larger linear fitting value (S_w) of Fe_2O_3-S/ACC after cycling test. The EIS results demonstrated the harder ion transfer of Fe_2O_3-S/ACC after cycling test, possibly due to the morphologies changes after cycling test as demonstrated above, leading to its capacitance loss.

In conclusion, although the charge transfer resistance and contact resistance of the two electrodes decreased after cycling test, a sheet-like structure generated at the surface of Fe_2O_3-S/ACC that was not conducive to ion migration, leading to an increase in the overall impedance in the

low-frequency region. Moreover, a more severe dissolution of active materials was observed in Fe$_2$O$_3$-S/ACC as demonstrated by ICP results. Therefore, based on the above results, it was reasonable to deduce that the dissolution of Fe$_2$O$_3$ and the harder ion migration were the main reason for the capacity degradation of Fe$_2$O$_3$-S/ACC electrode.
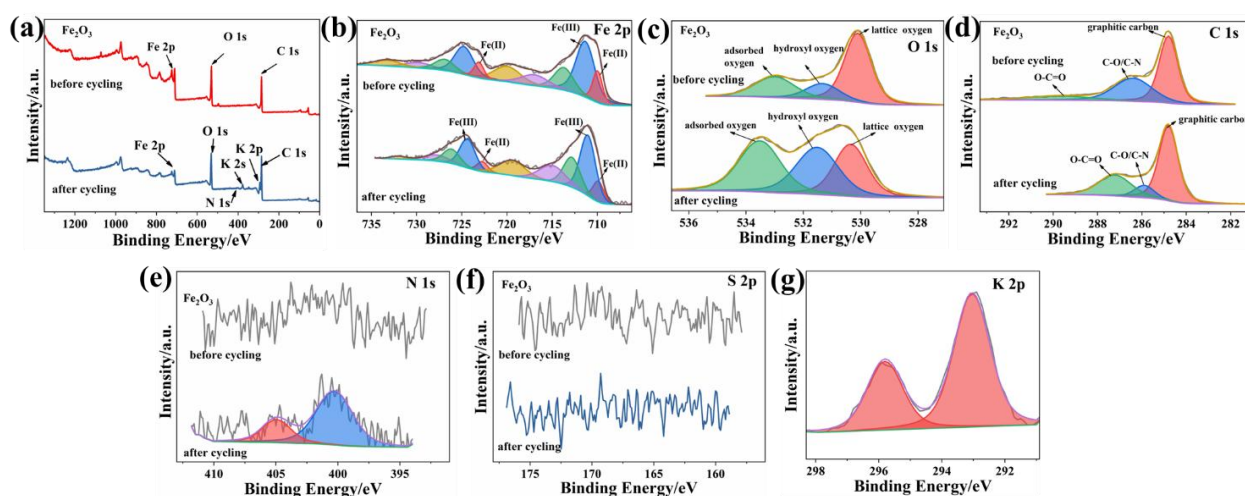

Fig. S12 XPS of Fe$_2$O$_3$/ACC before and after cycling test. (a) XPS survey; (b) Fe 2p; (c) O 1s; (d) C 1s; (e) N 1s; (f) S 2p; (g) K 2p.

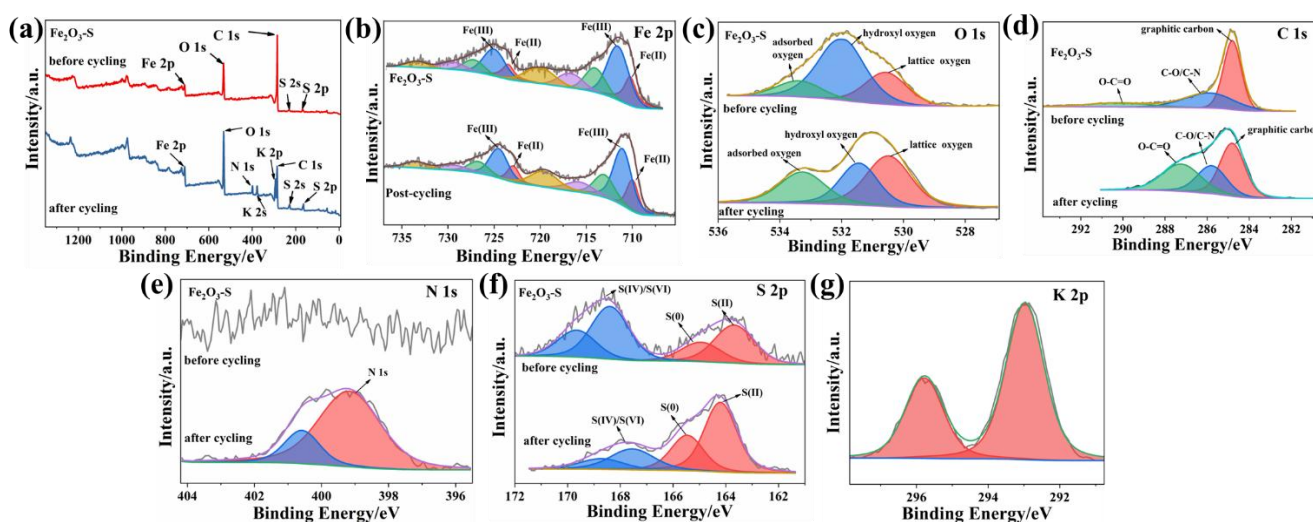**Fig. S13** XPS of Fe$_2$O$_3$-S/ACC before and after cycling test. (a) XPS survey; (b) Fe 2p; (c) O 1s; (d) C 1s; (e) N 1s; (f) S 2p; (g) K 2p.

Additionally, to further investigate the elemental composition and chemical states after cycling tests, XPS analysis was carried out and the results were shown in Fig. S12 and S13). From the XPS survey results (Fig. S12a and Fig. S13a), it could be seen that Fe, O, C, N and K elements were detected in both samples after cycling test, where K was originated from the KOH electrolyte. The K 2p spectra could be resolved into two peak components with binding energies at around 293 eV and 295 eV. These two peak components are associated with the spin-orbit split doublet (K 2p3/2and K 2p1/2, respectively) of the potassium ions. For both samples, no typical binding energy of metal nitrides (about 396-397 eV) was observed, therefore the fitting results of N 1s spectra after cycling tests demonstrated the N species (N–N, N–H, O–N) adsorbed at the surface of substrate.[2-4] Besides, the binding energies of Fe showed a negative shift after cycling test in both samples, suggesting that an electron rich structure induced by the delocalized electrons after cycling tests, which was in well agreement with the EIS results (Fig. 11a) as evidenced by the smaller R_s values after cycling tests for both samples. Additionally, the areas ratio of Fe^{2+}/Fe^{3+} in both samples slightly decreased (Fe_2O_3/ACC: 0.29 to 0.23; Fe_2O_3-S/ACC:0.37 to 0.34), implying the increased amount of Fe^{3+} after cycling due to the oxidation at the surface. For Fe_2O_3/ACC, it was obvious that the intensity of peaks representing oxygen and carbon-containing functional groups (OH⁻, Oads, O-C=O) in O 1s and C 1s spectra increased after cycling test, which was attributed to the high surface wettability and activity after cycling test. Similar results were obtained for Fe_2O_3-S/ACC by comparing the C 1s spectra before and after cycling test. Notably, unlike the dominance of OH⁻ and Oads in Fe_2O_3/ACC after cycling test, the lattice oxygen dominated in Fe_2O_3-S/ACC, which was probably attributed to the dissolution of S into electrolyte and decreased oxygen-sulfur groups at the surface after cycling test as evidenced by the S 2p spectra in Fig. S13f.

Table S6 XPS fitting parameters and results of Fe_2O_3, Fe_2O_3-S, Fe_2O_3 post-cycling and Fe_2O_3-S post-cycling.

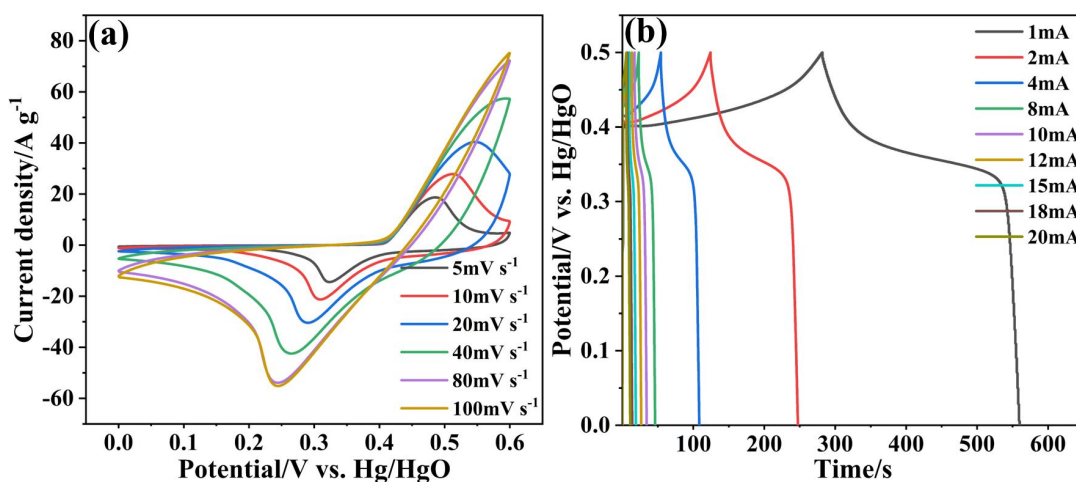| Sample / Fitting peaks	Fe_2O_3 (eV)	Fe_2O_3-S (eV)	Fe_2O_3 post-cycling (eV)	Fe_2O_3-S post-cycling (eV)
Fe(III) of Fe 2p 1/2	724.77	725	724.37	724.5
Fe(III) of Fe 2p 3/2	711.33	711.58	711.05	711.07
Fe(II) of Fe 2p 1/2	723.11	723.47	722.72	722.92
Fe(II) of Fe 2p 3/2	709.98	710.24	709.89	709.98
O 1s (lattice oxygen)	530.1	530.57	530.35	530.48
O 1s (hydroxyl oxygen)	531.33	531.94	531.52	531.44
O 1s (adsorbed oxygen)	533	533.37	533.52	533.27
C 1s (graphitic carbon)	284.8	284.8	284.8	284.8
C 1s (C-O/C-N)	286.4	285.89	285.89	285.78
C 1s (O-C=O)	289.64	290.17	287.21	287.22
S(-II) of S 2p 3/2	/	163.65	/	164.2
S(0) of S 2p 1/2	/	164.95	/	165.46
S(IV)/S(VI)	/	168.6	/	167.76
N 1s	/	/	400.29	399.17
N 1s	/	/	404.93	400.58
K 2p 3/2	/	/	293.04	292.97
K 2p 1/2	/	/	295.08	295.78

Fig. S14 The CV and GCD curves of NiCo-PBA electrode in three-electrode cell with Pt metal as the counter electrode and Hg/HgO as the reference electrode, respectively. 1 M KOH was employed as electrolyte.

The Fe_2O_3-S/ACC//NiCo-PBA asymmetric supercapacitor (ASC) device was assembled with 1 M KOH as the electrolyte and glass fiber paper (Whatman) as separator. The thickness of the Fe_2O_3-S/ACC, NiCo-PBA and the glass fiber paper was about 0.3 mm, 0.3 mm and 0.4 mm, respectively. Therefore, the total thickness of the device was about 1 mm. Besides, a three-electrode cell test was conducted for NiCo-PBA electrode and the CV and GCD results were shown in Fig. S14. It could be seen that NiCo-PBA electrode showed distinct redox peaks in the voltage window of 0-0.6 V at the scan rates of 5-20 mV s^{-1} and it could not present a complete pair of redox peaks at higher scan rates due to the severe polarization and irreversible reaction of the electrode. The GCD curves showed triangular-like curve with a charging and discharging platform which was corresponded to the redox peaks in the CV curves. Based on the above results, it was reasonable to deduce that the Fe_2O_3-S/ACC negative electrode was active in the voltage range from 0 V to 0.8 V and the NiCo-PBA positive electrode was active between 0.8 V to 1.5 V.

Fig. S15 Image of Fe$_2$O$_3$-S/ACC//NiCo-PBA ASC device that lighted a serious of LEDs

Table S7 Comparison of electrochemical performance tested in a three-electrode cell with reported literatures.

Sample	Aqueous electrolyte	Specific capacity	Rate capacity	Cycling performance	Ref.
Fe$_2$O$_3$/ACC	**1M KOH**	**551.54 mF cm^{-2} (2 mA cm^{-2})**	**55.19%, 2-25 mA cm^{-2}**	**No degradation (10000 cycles), 10 mA cm^{-2}**	**This work**
Fe$_2$O$_3$-S/ACC	**1M KOH**	**1465.26 mF cm^{-2} (2 mA cm^{-2})**	**59.06%, 2-25 mA cm^{-2}**	**72.51% (5000 cycles), 71.93% (10000 cycles), 10 mA cm^{-2}**	**This work**
Fe$_2$O$_3$ NTs@ppy/CC	1M Na$_2$SO$_4$	237mF cm^{-2} (1 mA cm^{-2})	43.04%, 1-20 mA cm^{-2}	80% (10000 cycles), 10 mA cm^{-2}	5
NCW@Fe$_2$O$_3$	3M KOH	603 F g^{-1} (0.1 A g^{-1})	67.2%, 0.1-50 A g^{-1}	85.5% (10000 cycles), 10 A g^{-1}	6
Fe$_2$O$_3$ NDs/RGO	2 M KOH	347 F g^{-1} (1 A g^{-1})	53.03%, 1-10 A g^{-1}	93.6% (2500 cycles), 5 A g^{-1}	7
Fe$_2$O$_3$@CNFs-rGO	6 M KOH	488 F g^{-1} (2 A g^{-1})	39.75%, 1-20 A g^{-1}	83.5% (5000 cycles), 4 A g^{-1}	8
Fe$_2$O$_3$@VN/CC	1M KOH	318.5 mF cm^{-2} (5 mA cm^{-2})	60%, 5-16 mA cm^{-2}	91.6% (5000 cycles), 20 mA cm^{-2}	9
Fe$_2$O$_3$/CC	1M LiOH	1.96 F cm^{-2} (1 mA cm^{-2})	42.86%, 1-20 mA cm^{-2}	93.5% (5000 cycles), 20 mA cm^{-2}	10
D-Fe$_2$O$_3$@PPy/CC	1M Na$_2$SO$_4$	615 mF cm^{-2} (1 mA cm^{-2})	33.82%, 1-20 mA cm^{-2}	79.3% (5000 cycles), 10 mA cm^{-2}	11
Co-Fe$_2$O$_3$@CC	1M Na$_2$SO$_4$	315.6 mF cm^{-2} (1 mA cm^{-2})	/	/	12
CC/Fe$_2$O$_3$@C-HASs	6 M KOH	1712.1 mF cm^{-2} (5 mA cm^{-2})	61.81%, 5-100 mA cm^{-2}	87.2% (5000 cycles), 20 mA cm^{-2}	13

References:

1. C. Guan, J. Liu, Y. Wang, L. Mao, Z. Fan, Z. Shen, H. Zhang and J. Wang, *ACS Nano*, 2015, **9**, 5198-5207.
2. A. M. Dmitrachkov, R. I. Kvon and A. V. Nartova, *Applied Surface Science*, 2021, **566**, 150631.
3. Z. Huang, Q. Zhou, J. Wang and Y. Yu, *Journal of Materials Science & Technology*, 2022, **112**, 68-76.
4. M. Guo, G. Q. Lu, X. Zhu, C. Wu and L. Wang, *Colloids and Surfaces A: Physicochemical and Engineering Aspects*, 2012, **395**, 100-104.
5. Y. Wang, Z. Du, J. Xiao, W. Cen and S. Yuan, *Electrochimica Acta*, 2021, **386**, 138486.
6. G. Duan, H. Zhang, C. Zhang, S. Jiang and H. Hou, *Chinese Chemical Letters*, 2023, DOI: 10.1016/j.cclet.2023.108283.

7. C. Wu, Z. Zhang, Z. Chen, Z. Jiang, H. Li, H. Cao, Y. Liu, Y. Zhu, Z. Fang and X. Yu, *Nano Research*, 2020, **14**, 953-960.

8. S. Jiang, J. Ding, R. Wang, Y. Deng, F. Chen, M. Zhou, H. Gui, X. Li and C. Xu, *Chemical Engineering Journal*, 2022, **431**, 133936.

9. H. Zhou, M. Alam, Y. Wu, Y. Zeng, A. N. Gandi, J. Zheng, W. Zhu, Z. Wang and H. Liang, *ACS Appl Mater Interfaces*, 2023, **15**, 18819-18827.

10. K. Li, B. Zhao, J. Bai, H. Ma, Z. Fang, X. Zhu and Y. Sun, *Small*, 2020, **16**, 2001974.

11. C. Wu, Z. Pei, M. Lv, D. Huang, Y. Wang and S. Yuan, *Molecules*, 2023, **28**, 434.

12. W. Shao, M. Li, X. Wang, N. Fu and Z. Yang, *Journal of Alloys and Compounds*, 2022, **929**, 167141.

13. Y. Wei, C.-M. Zhou, X.-M. Cao, Z.-J. Sun, Q. Wu, D.-L. Liu, Z. Xing and Q.-G. Zhang, *Journal of Alloys and Compounds*, 2022, **929**, 167245.